2H-Si/Ge for Group-IV Photonics: on the Origin of the Extended Defects in Core-Shell Nanowires

Fabrizio Rovaris,[†] Wouter H.J. Peeters,[‡] Anna Marzegalli,[†] Frank Glas,[¶] Laetitia Vincent,[¶] Leo Miglio,[†] Erik P.A.M. Bakkers,[‡] Marcel A. Verheijen,[*,‡] and Emilio Scalise[*,†]

[†]*Department of Materials Science, University of Milano Bicocca, 20125 Milan, Italy*

[‡]*Eindhoven University of technology, 5600 Eindhoven, the Netherlands*

[¶]*Université Paris-Saclay, CNRS, Centre for Nanoscience and Nanotechnology, Palaiseau 91120, France*

E-mail: m.a.verheijen@tue.nl; emilio.scalise@unimib.it

Abstract

The nucleation mechanism of ubiquitous basal stacking faults observed in hexagonal Si/Ge nanowires is still an enigma. These defects may hinder the exploitation of hexagonal Si/Ge for nano-opto-electronics and quantum technologies. In this work, the formation of the I_3 basal stacking faults is investigated at the atomistic level and results are compared to the experimental findings. We propose that these extended defects are caused by dislocation lines elongated in $\langle 11\bar{2}0 \rangle$ directions, which in turn arise from glide terminations of the step edges when two growing fronts run into each other.

Keywords

Hexagonal diamond SiGe, SiGe nanowires, I_3 defect, Machine Learning Interatomic Potentials, basal stacking faults, partial dislocations

Introduction

The enormous advances in nano-opto-electronics and quantum technologies are accompanied by the demand for high-quality materials and precise control of the growth process.[1–4] Crystalline defects may not only degrade the performances of the devices but often lead to their complete failure.[5] Understanding the mechanisms driving the formation of crystalline defects is the first step to engineering defect-free materials.[6–9] Recently, hexagonal diamond (2H) SiGe has been synthesized by exploiting core/shell nanowires[10–12] and demonstrating the direct electronic bandgap for the Ge-rich 2H-SiGe shells.[1] Thus, 2H-SiGe may contribute to the ongoing efforts to implement monolithically integrated optoelectronics.[13] However, because of the meta-stability of the 2H crystal phase, the inclusion of the most stable diamond cubic phase, which differs only for the different stacking sequences along the [111] direction, is easily understandable. In fact, the I_3 defect[14,15] is very often present in the 2H-SiGe shell and has been analysed in a couple of recent works.[16,17] A mechanism for its formation has been proposed, based on the experimental analysis but without any atomistic modelling support. Here, we propose in detail the general atomistic mechanism leading to the formation of the I_3 defect (I_3-BSF and its defect boundaries), in all the configurations observed so far, including non-triangular extended defects, shown here for the first time.

Results and discussion

The triangular I_3 defect in 2H-Ge nanowires has been analyzed by Fadaly et al.,[16] characterizing both its structural and electronic properties. Their investigation performed by transmission electron microscopy (TEM) studies imaging the nanowires along two different zone axes demonstrates that a basal stacking fault (I_3-BSF) is extended on a triangular area closed by the free surface and, on the other two sides, by two dislocation pairs with an angle of 60° between them. The I_3-BSF causes an altered stacking sequence ABCBA in the hexagonal (2H) ABAB sequence with the two pairs of opposite 30°-type partial dislocations along $\langle 11\bar{2}0\rangle$ directions bounding the stacking fault and allowing for the change in the dumbbell orientation. On both sides of the C-plane, which is replacing an A-plane, the crystal remains perfect, i.e., unshifted and undeformed because of the null total Burgers vector of the dislocation complexes. This evidence also indicates that the origin of the defect has not to be ascribed to strain relaxation processes.

Another recent work by Vincent et al.[17] added information on the occurrence of triangular I_3 defects as a function of the growth parameters and proposed a possible scenario for the origin of I_3 triangles. In particular, the authors indicate the presence of point defects located at the apex of the triangle as the most probable cause of the defect formation. However, in the same paper, the presence of I_3 defects that could not be explained by a triangular shape was also mentioned. Their shape implies that they should have a different formation mechanism. It is clear from Ref.[17] that the growth of the nanowire shell proceeds via step flow in the [0001] direction, with growth fronts on the $\{1\bar{1}00\}$ nanowire facets that appear more straight or meandered, depending on the deposition flux and temperature.

The $(1\bar{1}00)$ surface has been theoretically studied both for 2H-Si and Ge,[18,19] and it has the lowest surface energy on the $(1\bar{1}00)$ planes exhibiting a so-called shuffle surface reconstruction. However, glide terminations are also possible, although the glide $(1\bar{1}00)$ planes have higher surface energy compared to the shuffle ones.[18] Glide and shuffle name some specific $(1\bar{1}00)$ plane giving rise to the surface by cutting the crystal at two different positions and breaking the interatomic bonds inclined or orthogonal to the $(1\bar{1}00)$ plane,

respectively.[18] The hierarchy in the energy of the shuffle and glide terminations changes when looking at the surface steps. Considering a step edge on the $(1\bar{1}00)$ surface, two different step configurations are possible for step edges parallel to the $\langle 11\bar{2}0\rangle$ direction, as shown in Figure 1(a) and (b). These two configurations differ for the termination of the plane containing the step being glide or shuffle, respectively. While the top view (i.e. a section orthogonal to the [0001] direction) of the former shows five-rings alternated with open four-rings, only six-rings are present in the shuffle termination. Our *ab initio* calculations based on the density functional theory (DFT)[20–23] evidence that the glide step termination (Figure 1(a), green atoms) is more energetically favourable by 67 meV/Å for Ge (11 meV/Å for Si) as compared to the shuffle step termination (Figure 1(b)). As a consequence, any step edge parallel to the $\langle 11\bar{2}0\rangle$ direction is expected to have more likely glide termination. Details of the *ab initio* calculations are provided in the Methods section of the Supporting Information.

To shed light on the mechanism giving rise to I_3 defects, it is necessary to focus on the collision of growing fronts, which we will assume always as step edges parallel to the $\langle 11\bar{2}0\rangle$ direction, with the glide reconstruction discussed above. This includes two possible scenarios: Firstly, two bilayer kinks moving in two opposite $\langle 11\bar{2}0\rangle$ directions are merging while completing an $\{0002\}$ atomic layer (see Fig. 1(c)); Secondly, two growth fronts propagating on the sidewalls of the nanowire in two opposite $\langle 0001\rangle$ directions create a straight junction elongated in the $\langle 11\bar{2}0\rangle$ direction, lying on the sidewalls of the nanowire (see Fig. 1(d)). As we will show below, the former leads to the formation of the triangular I_3 defects, while the latter allows for other geometries of the I_3 defect. Let us start the discussion from the former case, schematically illustrated in Figure 1(c). The corresponding atomistic views of the process are shown in Fig. 2(a): two $\langle 11\bar{2}0\rangle$ bilayer kinks with the same glide reconstruction discussed above (green atoms in the figure) join together. Atoms are incorporated on the growing front till the steps reach each other. If an atom not belonging to the glide reconstruction of the two merging steps (red-circled atom in Fig. 2(a)) is added near the

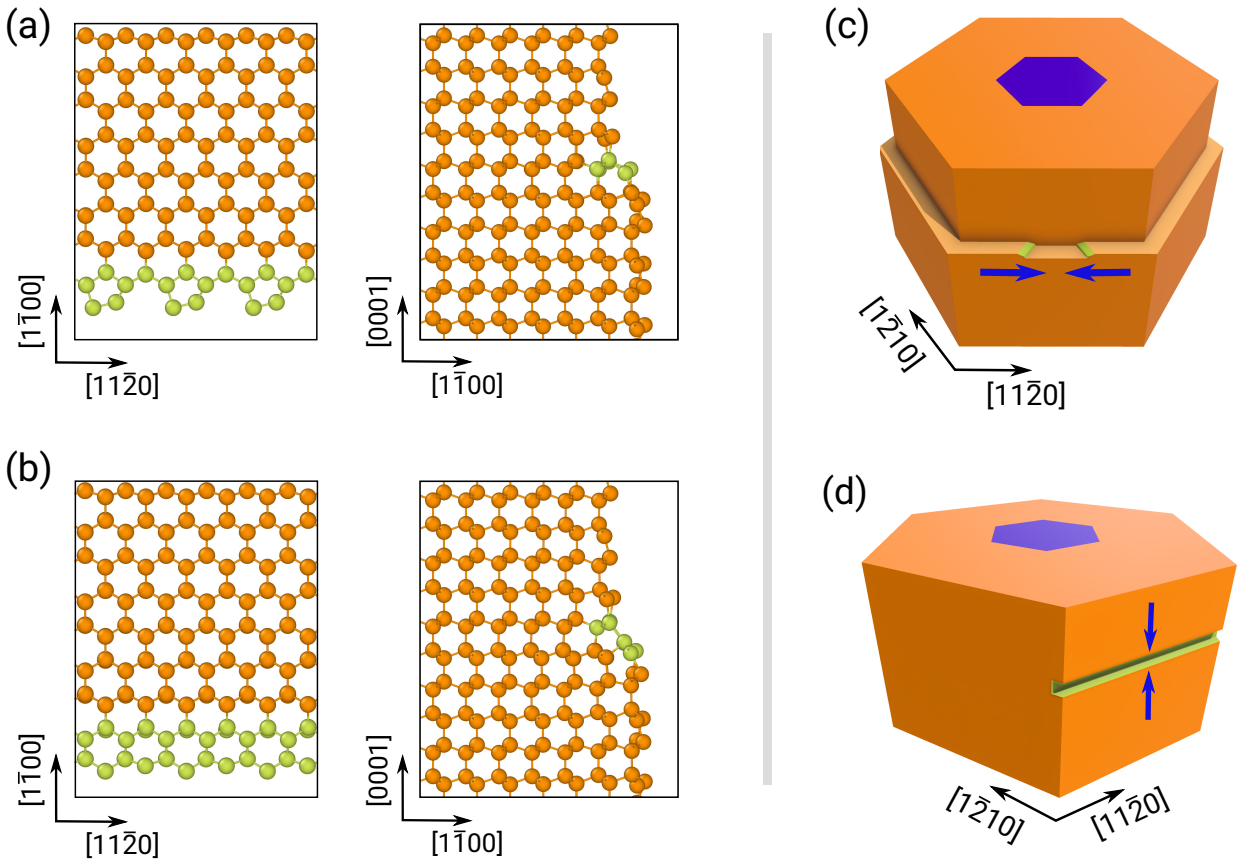

Figure 1: Glide (a) and shuffle (b) termination of the step edge. The top views in the two panels show only the atomic layer containing the step edge. The side view is shown with plane normal direction $\langle 11\bar{2}0\rangle$. In all panels atoms belonging to the step reconstruction are highlighted in green. (c) Sketch of the first possible step merging during the growth: two steps flow along one of the nanowire sidewalls as highlighted by the blue arrows. (d) Sketch of the second possible step merging: two growing fronts merge on one nanowire sidewall in the area shaded in yellow, along the [0001] direction.

initial meeting point, it closes an open ring of the glide termination forming seven/five-rings, which stabilize such reconstruction at the meeting point. Calculations performed exploiting a Machine Learning (ML) interatomic potential (GAP[24]) show that such configuration is energetically stable. Moreover, we evaluated the energy of the same number of atoms arranged in six-rings, thus corresponding to a bulk-like configuration (shown in the Supporting Information, Figure S7, and it turns out to be higher by about 0.67 eV for silicon, confirming the higher stability of the configuration with seven/five-rings. We also investigated via the Nudged Elastic Band (NEB) procedure[25] the Minimum Energy Path (MEP) and the relative energy barrier connecting the two configurations (see Figure S7). We can conclude that, after merging the two steps, the apex structure composed of seven- and five-rings is stable and thus may be kept embedded into the shell. At the subsequent stage of the growth, other atomic rings are also closed as eight- and five-rings, giving rise to the structure reported in the last panel of Figure 2(a), being also stable after energy minimization. Continuing with the growth, the next atomic layer in the [0001] direction (normal to the plane of the paper) is placed. This completes the apex with a second atomic layer arranged in seven- and five-rings placed in an alternated manner as compared to the first one. This structure is illustrated in the left panel of Fig. 2(b) showing the two atomic layers overlapping in the [0001] direction. Such configuration corresponds exactly to the triangular I_3 defect reported in Ref.:[16] two pairs of 30° partial dislocations along $\langle 11\bar{2}0\rangle$ directions surrounding an I_3-BSF. We investigated the stability of the defect at this growth stage by performing NEB calculation of the MEP connecting the defected structure with the perfect 2H-Si crystal (second panel in Fig. 2(b)). A proper set of configurations taken along the MEP is shown in the Supporting Information (Figure S9) and the whole process is also shown in Supplementary Movie 1. The corresponding energy plot is illustrated in Fig. 2(c), showing that, while the perfect crystal is energetically more stable, an energy barrier of about 50 meV is present between the two configurations, thus indicating a certain stability of the faulted structure at the growing temperature. Note that in this energy barrier calculation, we account only

for the minimum possible length of the growth fronts because the calculations become too complex for longer fronts, but the barrier is expected to increase substantially. Indeed, such a conclusion can also be drawn by looking at the Molecular Dynamics (MD) simulations reported in Supplementary Video 2 and 3, where we show the annealing (at the temperature of 900 K) of the defected structure at growth stages 2 and 3, respectively. The movies show that the defected structure at growth stage 2 transforms back to the perfect crystal after some time of the simulation ($\sim$ 200 ps), while the defected structure at growth stage 3 remains stable up to the end of the simulation (800 ps).

Continuing our discussion by considering the nanowire sidewall advancing in the radial $\langle 1\bar{1}00\rangle$ direction, the structure continues the eight- and five-rings like reported in the two panels of Fig. 2(d), which shows the growth stages 5 and 15, respectively. These eight- and five-rings border the region between the hexagonal 2H structure and the faulted cubic one (orange and blue atoms in the figure, respectively). Figure 2(e) shows the formation energy values computed at different growth stages, i.e. adding atomic layers in the radial direction, to the triangular defect. It is evident that the gain in energy due to the insertion of two cubic planes in the stacking fault overcomes the energy cost of the dislocations after growth stage 15 (about 5 nm in the radial direction) making the faulted structure thermodynamically more stable than the pristine crystal after this point. These considerations on the thermodynamic stability of the defect are supported by the MD simulations of the triangular defect described above and fully reported in the Supporting Information.

Summarizing the results obtained so far, the merging of two steps during the epitaxial growth may give rise to the triangular defect. This finding is in agreement with the experimental evidence reported in Ref.[17] where the defect density is shown to be increased, with increasing surface roughness and decreasing temperature. Indeed, our results show that the probability of maintaining a defected configuration is enhanced in the case of longer fronts in the radial directions, higher frequency of meeting events between different growing fronts (i.e. increased surface roughness, more nuclei per facet, meandering of the step edges) and

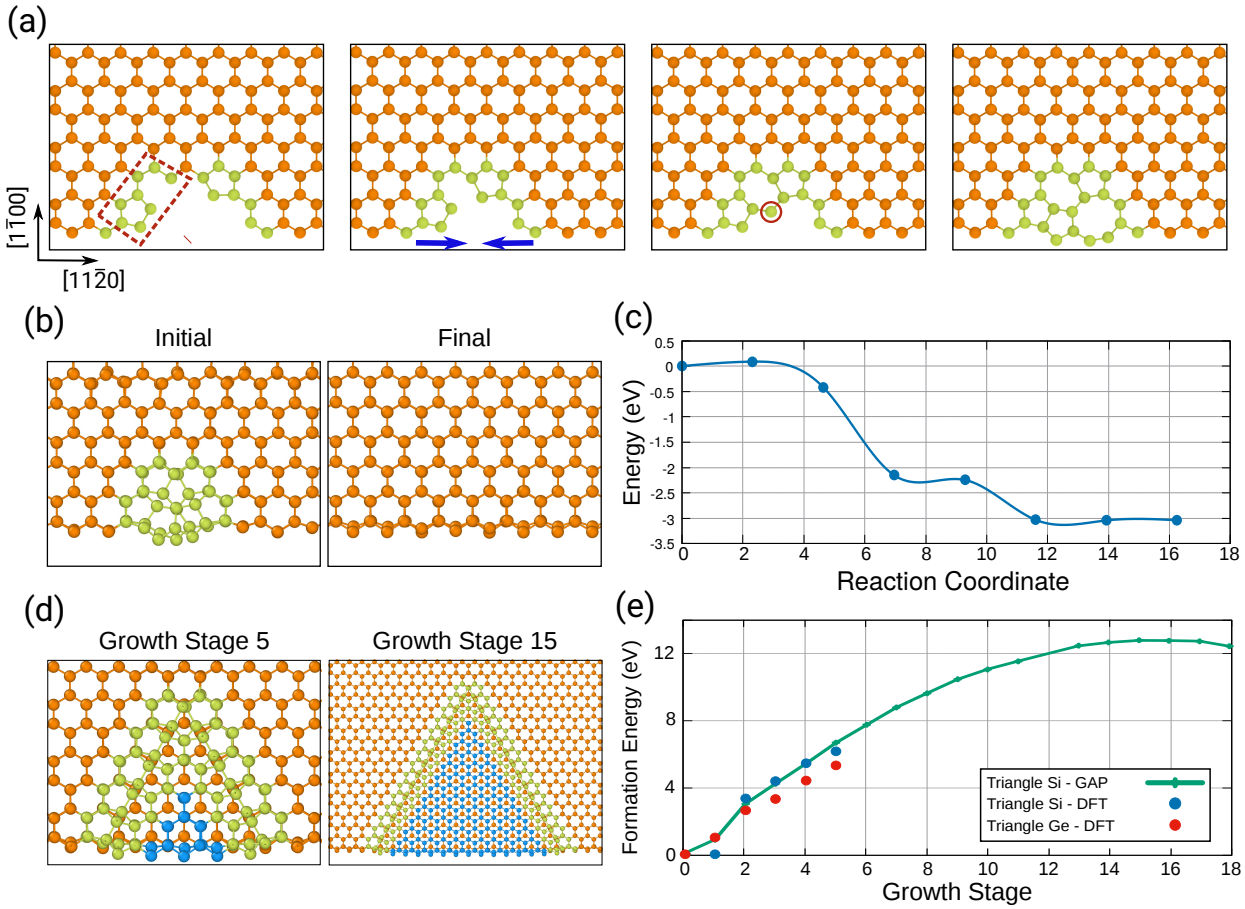

Figure 2: (a) Atomistic model of the two steps merging shown as a top view of the single atomic layer containing the steps. The red box highlights the glide termination of one of the two step edges. Both step edges are elongated in the $\langle 11\bar{2}0 \rangle$ direction. The red-circled atom stabilizes the 7/5 rings constituting the apex of the I_3 defect. (b) The origin of the I_3 defect as a result of the merging of two glide-terminated steps (first panel) and the perfect 2H-Si crystal (second panel). Note that here two atomic layers containing the defect are shown. (c) NEB calculation of the MEP connecting the two configurations shown in (b), calculated exploiting the GAP potential. The potential energy is calculated as the energy variation from the initial (defected) to the final (non-defected) configuration and considers a few snapshots along the transition path. (d) Two examples of the triangular I_3 defect at different growth stages, 5 and 15, respectively. (e) Formation energy of the I_3 defect as a function of the growth stage. "Stage 0" represents the configuration without any defect. The formation energy of Si is obtained by exploiting the GAP potential, but for the initial growth stages, DFT results are also shown both for Si and Ge. The orange colour identifies atoms in the hexagonal diamond configuration, the green colour identifies atoms belonging to the dislocation, while blue is for the cubic diamond.

lower temperatures. The latter is related to the fact that the probability of overcoming the energy barrier to break up a defect configuration and restore the perfect crystal is (exponentially) dependent on the temperature. Eventually, in the case of a layer-by-layer growth mode of single-step fronts, observed at low supersaturation and high temperature, no merging of bilayer kinks will occur and, in principle, one would expect no defects.

Our results point out the merging of steps with glide termination as the origin of the I_3 defect while excluding point defects. In fact, we have performed simulations of the hexagonal crystal including a point-like defect at the shuffle surface and, as further discussed in the Supporting Information, both for Si and Ge the structures analyzed are not stable and would transform back to the perfect crystal with no energy barrier. Thus, even if for any reason the point defect was embedded in the structure forming the very early stage of the I_3 apex, then it would immediately transform into a perfect 2H crystal at the growth temperature. Finally, the investigation of GaAs/Ge-2H nanowires, with the Ge shell obtained by Molecular-beam epitaxy (MBE) confirmed the presence of I_3 defects in the shell. By exploiting this low impurity growth mode, we exclude extrinsic defects as a possible origin of the I_3 defect (see experimental details and Figure S6 in the Supporting Information). Thus, the hypothesis that has been previously proposed for the formation of the I_3 triangular defect,[17] assuming its origin as a point defect embedded in the radial growth of the shell, is excluded by the current experimental and theoretical analysis.

Now let us discuss the case of junctions formed by growing fronts on the $\{1\bar{1}00\}$ nanowire facets that propagate in opposite $\langle 0001\rangle$ directions, as schematically depicted in Figure 1(d). Such a configuration consists of two step edges parallel to $\langle 11\bar{2}0\rangle$, each one exhibiting a glide reconstruction like the one in Fig. 1(a). After the merging, the resulting configuration has been analyzed both by the DFT and MD simulations and named "growth stage 1" in the following. The formation energy is estimated as 80 meV/Å (102 meV/Å) for Ge(Si). This formation energy is relatively low: the energy cost of a few nanometers of this line defect is lower than that of a single neutral vacancy.[26] More importantly, our classical MD

simulations (details are reported in Supporting Information) show that it is very stable after several hundred picoseconds of annealing at high temperatures (900 K for Silicon). When a next bilayer grows in the radial $\langle 1\bar{1}00\rangle$ direction, the line will be mirrored with the axes along the $\langle 11\bar{2}0\rangle$ direction, giving rise to a line defect corresponding to a pair of 30° partial dislocations (Figure 3(a)). Our MD simulations evidence the stability of the dislocation line also at this stage (see Supporting Information). Moreover, the formation energy of this elongated defect (see Table 1), after a slight increase as the core of the dislocation is completed, decreases with the shell thickness, as reported in Fig. 3(e) for the elongated defects both in Si and Ge. This is due to the lower cohesion energy of the double cubic staking formed after the dislocation core in the $\langle 1\bar{1}00\rangle$ direction and highlighted by blue colour in Figure 3(a)-(d) for different growth stages. Therefore, while the nanowire grows in the radial directions, the defected area expands in the $\langle 1\bar{1}00\rangle$ direction. As a consequence, the cubic bilayer (blue area in Figure 3(a)-(d)) expands in the $\langle 1\bar{1}00\rangle$ direction.

Table 1: Formation energy of the elongated dislocation line in Si and Ge meV/Å

Description	Ge	Si
Stage 1, half of the dislocation line is formed	80	102
Stage 2, the dislocation line is formed	139	202
Stage 3, the dislocation line is formed plus an extra atomic layer	143	210
Stage 4, the dislocation line is formed plus 2 other atomic layers	126	196
Stage 5, the dislocation line is formed plus 3 other atomic layers	108	175

Our model based on the reconstruction of the step edge as a glide termination is thus able to explain the formation of the triangular I_3 defects but also of non-triangular ones, with dislocation lines parallel to the sidewalls of the nanowire.

The presence of non-triangular I_3 defects has been proven by TEM analysis. Beyond the typical triangular I_3 defects,[16,17] elongated defects with a projected length larger than the shell thickness have been observed. Figure 4 displays the in-plane geometry of such a defect in a $Si_{0.2}Ge_{0.8}$ shell in detail by combining views on the same defect from four different viewing orientations using a combination of bright field and annular dark field STEM. The details on the image contrast leading to the reconstruction of the shape are discussed to more

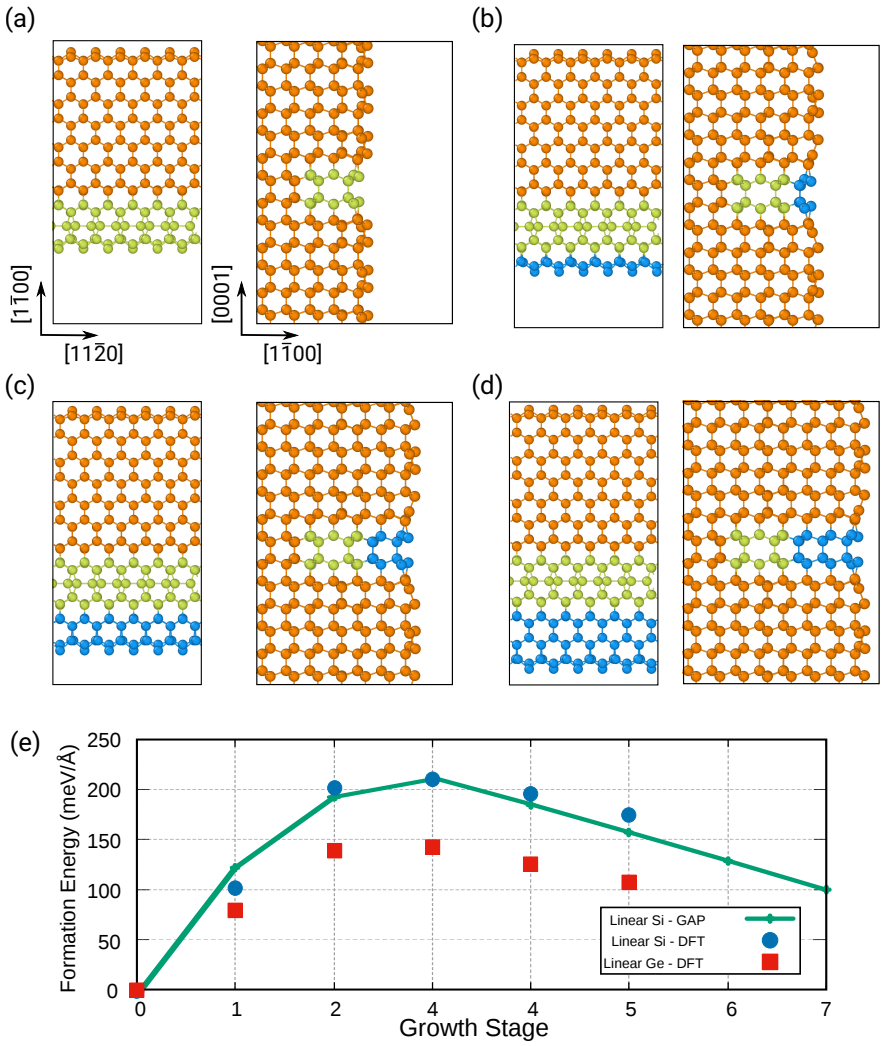

Figure 3: (a)-(d) Top (only two atomic layers are shown) and side view of the dislocation core at different growth stages, starting from stage 2. From (a) to (d), atomic layers are added along the $\langle 1\bar{1}00 \rangle$ direction. The orange colour identifies atoms in the hexagonal diamond configuration, the green colour identifies atoms belonging to the dislocation, while blue is for the cubic diamond. (e) Formation energy at different growth stages of a non-triangular I_3 defect with dislocation lines parallel to the NW sidewalls.

extent in the Supporting Information. The shape is clearly different from a triangle; rather, the defect covers more than one entire segment of the SiGe shell assuming a U-shape. Its inner boundary is the core-shell interface. The defect is bound by elongated defects as shown by the images in Figure 4. Within the same nanowire segment, 57 defects were studied. Of these, 14 had the previously reported triangular shape and had their apex somewhere in the SiGe shell. The other 43 were non-triangular defects. For 21 of these defects, the shape could uniquely be assigned: all had shapes extending along the core-shell boundary, covering at least one facet of the GaAs core, examples of these defects are presented in the Supporting Information. It should be mentioned that the dependence of the density of these two types of defects as a function of e.g. growth temperature and Si:Ge ratio has not been investigated and has to be done in further systematic studies of these nanowires.

From the atomistic point of view, U-shaped defects like those reported in Fig. 4(h) are composed of three segments of elongated defects with dissimilar core reconstructions. Indeed, whenever the elongated defect "turns" one corner of the nanowire with a 120° angle its core assumes a different atomistic structure switching among two possible crystal symmetries, as shown in Fig. 5(a). The atomistic details of the dislocation cores in panels (b) and (c) of Fig. 5 show the different core reconstruction for the two dislocation segments: the blue lines indicate a *flower* dislocation core (Fig. 5(b)), while the red lines a *butterfly* one (Fig. 5(c)). This nomenclature, as introduced in Ref.,[16] refers to the side view of the atomic arrangements of the defects (Fig. 5(b) and (c)), as they would emerge on the sidewall of the nanowire. We also computed the formation energy of the elongated defects in Fig. 5(b) and (c), and the results predict that the *butterfly* defect has formation energy more than double that one of the *flower* defect, 304 meV/Å (456 meV/Å) versus 139 meV/Å (202 mev/Å) as calculated by DFT for Ge (Si), respectively.

To exhaustively explain the different shapes of non-triangular defects observed in the experiments, one needs to go beyond the early origin of the I_3 defect and consider also the evolution (e.g. motion) of the defect during the growth. This will be discussed in detail in a

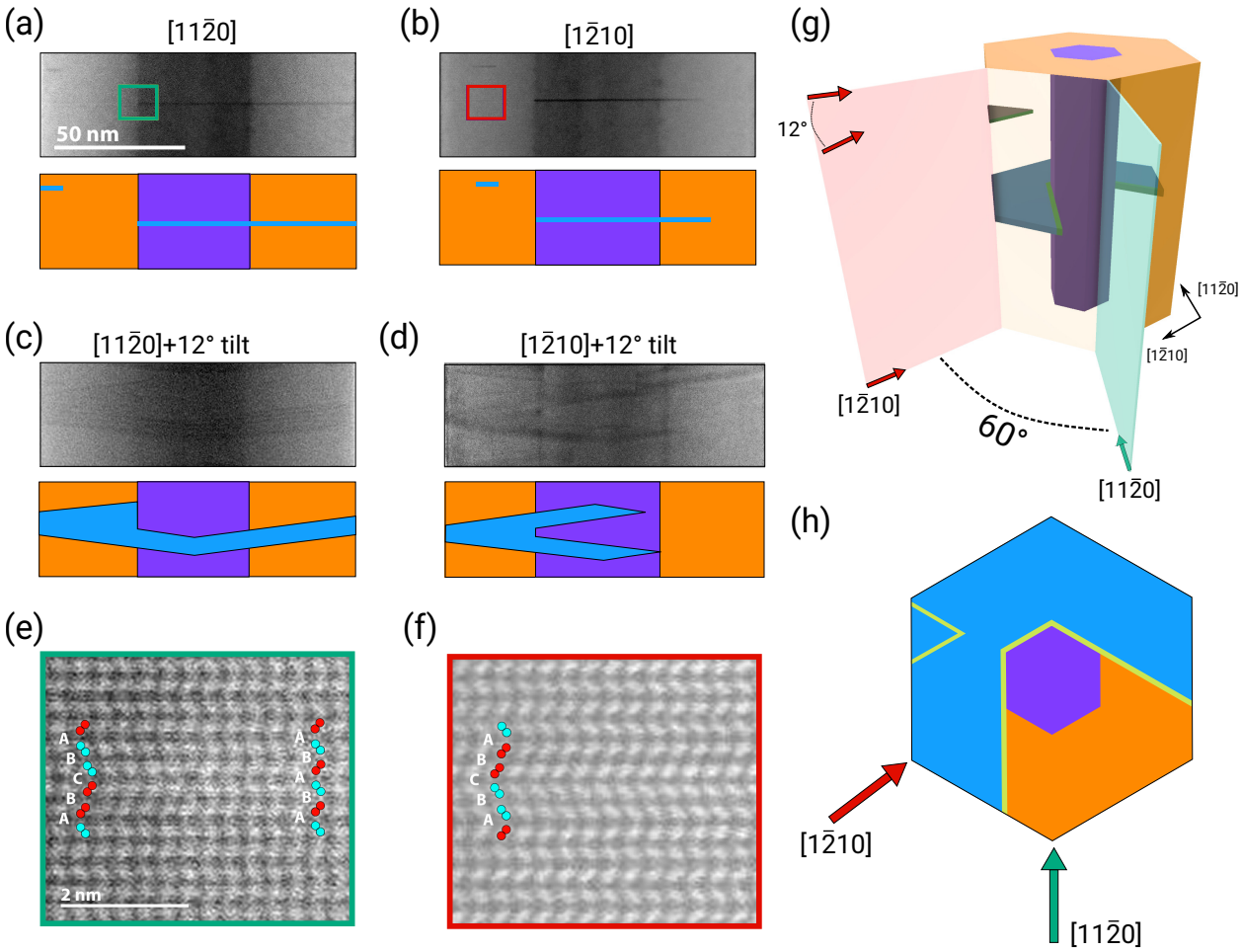

Figure 4: Scanning TEM study of a triangular I_3 defect and an extended I_3 defect within the SiGe shell. The same wire segment was imaged at 4 different viewing angles, as depicted in (g). Bright Field STEM images and accompanying cartoons display the angle-dependent contrasts. (a), (b) imaging orthogonal to the long axis of the nanowire, at two different $\langle 11\bar{2}0 \rangle$ zone axes, correlated by a 60° rotation around this long axis. (c), (d) tilted 12° off the axes normal to the nanowire, relative to the two [11$\bar{2}$0] zone axes. (e), (f) HAADF-STEM images of the positions indicated in (a), (b). In (e) an I_3 defect boundary is recognizable, in (f) the ABCBA I_3 stacking is visible. (g) 3D sketch representing the 4 different viewing axes. (h) reconstructed in-plane shape of the I_3 defects.

future work, devoted to the study of the kinetic mechanisms influencing these defects. Limiting the discussion to simple thermodynamic considerations, one can infer that the energy gain in extending the cubic bilayer over a certain dimension can overcome the energy cost of extending the elongated defects bounding the bilayer. Indeed, the former has a quadratic dependence on the size, while it is linear for the latter energy. These considerations are also valid when the elongated defect extends on more than a single facet of the nanowire, turning a nanowire corner, thus increasing the cubic area. The thermodynamic model reported in the Supporting Information shows that there exists a critical shell dimension for which this defect extension is favourable. This can be the reason for a backpropagation of the defect towards the nanowire core, wrapping around it. Notice that our thermodynamic model, fully reported in the Supplementary Material, predicts that the short segment of the U-defect embedded inside the shell assumes the butterfly core reconstruction. Indeed, the experimental observations of defects emerging at the surface, like Fig. 4(e), show the flower defect reconstruction. On the contrary, buried defects at the center of the nanowire can not be easily observed at atomic resolution in the STEM images, due to the limited depth of focus of the probe-corrected STEM mode.

Conclusions

In conclusion, we have shown how a generic property of these nanostructures, i.e. the surface reconstructions, influences the atomistic structure during the growth and may lead to the formation of extended defects. In particular, we show how the glide termination of the $(1\bar{1}00)$ 2H-Ge (or Si) surface may give rise to dislocation segments and basal stacking faulted planes, namely the I_3 defect. Thus, opposite to the apparently obvious and previously supposed point-like origin, the formation mechanism of these I_3 defects is identified in a line-like origin, explaining all the experimental pieces of evidence, including the unusual extended non-triangular I_3 defect.

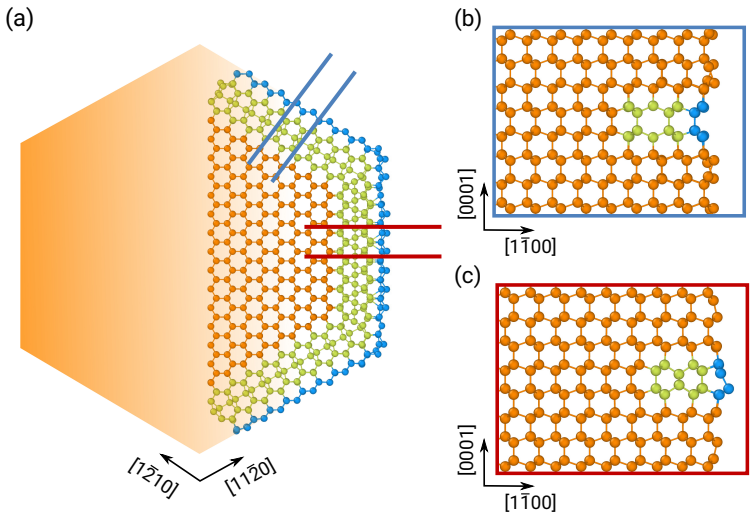

Figure 5: (a) Top view of the atomistic structure of a U-shaped defect running along the nanowire sidewalls. When a defect turns a corner with a 120° angle the dislocation line character changes from the *flower* defect (b) to the *butterfly* defect (c) and *vice versa*. The orange colour identifies atoms in the hexagonal diamond configuration, the green colour identifies atoms belonging to the dislocation, while blue is for the cubic diamond.

Supporting Information

- Additional experimental details and methods: materials synthesis, TEM characterization and additional images, including defect visualization. Additional atomistic simulations of the defects, thermodynamic considerations on their extension, and theoretical methods (PDF).

- Supp. Video 1: MEP connecting the triangular I_3 defected structure at growth stages 2 and the perfect 2H-Si crystal (AVI)

- Supp. Video 2: Classical MD simulation(at the temperature of 900 K) of the triangular I_3 defected structure at growth stages 2 (AVI)

- Supp. Video 3: Classical MD simulation(at the temperature of 900 K) of the triangular I_3 defected structure at growth stages 3 (AVI)

- Supp. Video 4: MEP connecting the triangular I_3 defected structure at growth stage 1 with the perfect crystal (AVI)

Acknowledgement

F.R. and E.S. acknowledge the CINECA consortium under the ISCRA initiative for the availability of high-performance computing resources and support. Solliance and the Dutch province of Noord Brabant are acknowledged for funding the TEM facility. E.B. acknowledges funding from the European Union's Horizon Europe research and innovation program under grant agreement number 964191 (Opto Silicon). We thank P.J. van Veldhoven and M.G. van Dijstelbloem for the technical support of the MOVPE reactor, and Mette Schouten for critical reading of the manuscript.

References

(1) Fadaly, E. M. T.; Dijkstra, A.; Suckert, J. R.; Ziss, D.; van Tilburg, M. A. J.; Mao, C.; Ren, Y.; van Lange, V. T.; Korzun, K.; Kölling, S.; Verheijen, M. A.; Busse, D.; Rödl, C.; Furthmüller, J.; Bechstedt, F.; Stangl, J.; Finley, J. J.; Botti, S.; Haverkort, J. E. M.; Bakkers, E. P. A. M. Direct-bandgap emission from hexagonal Ge and SiGe alloys. *Nature* **2020**, *580*, 205–209, Number: 7802 Publisher: Nature Publishing Group.

(2) Iyer, S. S.; Xie, Y. H. Light Emission from Silicon. *Science* **1993**, *260*, 40–46.

(3) de Leon, N. P.; Itoh, K. M.; Kim, D.; Mehta, K. K.; Northup, T. E.; Paik, H.; Palmer, B. S.; Samarth, N.; Sangtawesin, S.; Steuerman, D. W. Materials challenges and opportunities for quantum computing hardware. *Science* **2021**, *372*, eabb2823.

(4) Becher, C.; Gao, W.; Kar, S.; Marciniak, C. D.; Monz, T.; Bartholomew, J. G.; Goldner, P.; Loh, H.; Marcellina, E.; Goh, K. E. J.; Koh, T. S.; Weber, B.; Mu, Z.; Tsai, J.-Y.; Yan, Q.; Huber-Loyola, T.; Höfling, S.; Gyger, S.; Steinhauer, S.; Zwiller, V. 2023 roadmap for materials for quantum technologies. *Materials for Quantum Technology* **2023**, *3*, 012501.

(5) Giannazzo, F.; Greco, G.; Di Franco, S.; Fiorenza, P.; Deretzis, I.; La Magna, A.; Bongiorno, C.; Zimbone, M.; La Via, F.; Zielinski, M.; Roccaforte, F. Impact of Stacking Faults and Domain Boundaries on the Electronic Transport in Cubic Silicon Carbide Probed by Conductive Atomic Force Microscopy. *Advanced Electronic Materials* **2020**, *6*, 1901171.

(6) Scalise, E.; Barbisan, L.; Sarikov, A.; Montalenti, F.; Miglio, L.; Marzegalli, A. The origin and nature of killer defects in 3C-SiC for power electronic applications by a multiscale atomistic approach. *J. Mater. Chem. C* **2020**, *8*, 8380–8392.

(7) Barbisan, L.; Marzegalli, A.; Montalenti, F. Atomic-scale insights on the formation of ordered arrays of edge dislocations in Ge/Si(001) films via molecular dynamics simulations. *Scientific Reports* **2022**, *12*, 3235.

(8) Skibitzki, O.; Zoellner, M. H.; Rovaris, F.; Schubert, M. A.; Yamamoto, Y.; Persichetti, L.; Di Gaspare, L.; De Seta, M.; Gatti, R.; Montalenti, F.; Capellini, G. Reduction of threading dislocation density beyond the saturation limit by optimized reverse grading. *Phys. Rev. Mater.* **2020**, *4*, 103403.

(9) Montalenti, F.; Rovaris, F.; Bergamaschini, R.; Miglio, L.; Salvalaglio, M.; Isella, G.; Isa, F.; Von Känel, H. Dislocation-Free SiGe/Si Heterostructures. *Crystals* **2018**, *8*.

(10) Algra, R. E.; Hocevar, M.; Verheijen, M. A.; Zardo, I.; Immink, G. G.; Van Enckevort, W. J.; Abstreiter, G.; Kouwenhoven, L. P.; Vlieg, E.; Bakkers, E. P. Crystal structure transfer in core/shell nanowires. *Nano Letters* **2011**, *11*, 1690–1694.

(11) Hauge, H. I. T.; Verheijen, M. A.; Conesa-Boj, S.; Etzelstorfer, T.; Watzinger, M.; Kriegner, D.; Zardo, I.; Fasolato, C.; Capitani, F.; Postorino, P.; Kölling, S.; Li, A.; Assali, S.; Stangl, J.; Bakkers, E. P. A. M. Hexagonal Silicon Realized. *Nano Letters* **2015**, *15*, 5855–5860.

(12) Hauge, H. I. T.; Conesa-Boj, S.; Verheijen, M. A.; Koelling, S.; Bakkers, E. P. Single-Crystalline Hexagonal Silicon-Germanium. *Nano Letters* **2017**, *17*, 85–90.

(13) Barth, S.; Seifner, M. S.; Maldonado, S. Metastable Group IV Allotropes and Solid Solutions: Nanoparticles and Nanowires. *Chemistry of Materials* **2020**, *32*, 2703–2741.

(14) Zakharov, D. N.; Liliental-Weber, Z.; Wagner, B.; Reitmeier, Z. J.; Preble, E. A.; Davis, R. F. Structural TEM study of nonpolar a-plane gallium nitride grown on (11-20)4H-SiC by organometallic vapor phase epitaxy. *Physical Review B - Condensed Matter and Materials Physics* **2005**, *71*, 1–9.

(15) Stampfl, C.; Van de Walle, C. G. Energetics and electronic structure of stacking faults in AlN, GaN, and InN. *Physical Review B - Condensed Matter and Materials Physics* **1998**, *57*, R15052–R15055.

(16) Fadaly, E. M.; Marzegalli, A.; Ren, Y.; Sun, L.; Dijkstra, A.; De Matteis, D.; Scalise, E.; Sarikov, A.; De Luca, M.; Rurali, R.; Zardo, I.; Haverkort, J. E.; Botti, S.; Miglio, L.; Bakkers, E. P.; Verheijen, M. A. Unveiling Planar Defects in Hexagonal Group IV Materials. *Nano Letters* **2021**, *21*, 3619–3625.

(17) Vincent, L.; Fadaly, E. M.; Renard, C.; Peeters, W. H.; Vettori, M.; Panciera, F.; Bouchier, D.; Bakkers, E. P.; Verheijen, M. A. Growth-Related Formation Mechanism of I3-Type Basal Stacking Fault in Epitaxially Grown Hexagonal Ge-2H. *Advanced Materials Interfaces* **2022**, *9*.

(18) Béjaud, R.; Hardouin Duparc, O. Stabilizing the hexagonal diamond metastable phase in silicon nanowires. *Computational Materials Science* **2021**, *188*.

(19) Scalise, E.; Sarikov, A.; Barbisan, L.; Marzegalli, A.; Migas, D. B.; Montalenti, F.; Miglio, L. Thermodynamic driving force in the formation of hexagonal-diamond Si and Ge nanowires. *Applied Surface Science* **2021**, *545*, 148948.

(20) Perdew, J. P.; Burke, K.; Ernzerhof, M. Generalized Gradient Approximation Made Simple. *Physical Review Letters* **1996**, *77*, 3865–3868.

(21) Blöchl, P. E. Projector augmented-wave method. *Physical Review B* **1994**, *50*, 17953–17979.

(22) Kresse, G.; Furthmüller, J. Efficient iterative schemes for ab initio total-energy calculations using a plane-wave basis set. *Computational Materials Science* **1996**, *6*, 11169–11186.

(23) Kresse, G.; Joubert, D. From ultrasoft pseudopotentials to the projector augmented-wave method. *Physical Review B* **1999**, *59*, 1758–1775.

(24) Bartók, A. P.; Kermode, J.; Bernstein, N.; Csányi, G. Machine learning a general-purpose interatomic potential for silicon. *Physical Review X* **2018**, *8*, 041048.

(25) Henkelman, G.; Uberuaga, B. P.; Jónsson, H. A climbing image nudged elastic band method for finding saddle points and minimum energy paths. *The Journal of Chemical Physics* **2000**, *113*, 9901–9904.

(26) Pinto, H. M.; Coutinho, J.; Torres, V. J.; Öberg, S.; Briddon, P. R. Formation energy and migration barrier of a Ge vacancy from ab initio studies. *Materials Science in Semiconductor Processing* **2006**, *9*, 498–502.